Journal of ELECTRONIC MATERIALS, Vol. 44, No. 11, 2015
DOI: 10.1007/s11664-015-4016-x

Graphene–Inorganic Hybrids with Cobalt Oxide Polymorphs for Electrochemical Energy Systems and Electrocatalysis: Synthesis, Processing and Properties

SANJU GUPTA[1,3] and SARA B. CARRIZOSA[2]

1.—Department of Physics and Astronomy, Western Kentucky University, 1906 College Heights Blvd., Bowling Green, KY 42101-3576, USA. 2.—Department of Chemistry, Western Kentucky University, 1906 College Heights Blvd., Bowling Green, KY 42101-3576, USA. 3.—e-mail: sanju.gupta@wku.edu

We report on the synthesis and physical property characterization of graphene–inorganic 'hybrid' nanomaterials coupled with nano-/microscale transition metal oxide polymorphs namely, cobalt oxides, i.e. CoO [Co(II)] and Co_3O_4 [Co(II, III)]), for alternative energy storage and conversion devices. Their demand is owed to higher specific capacitance, wide operational potential window, stability through charge–discharge cycling, environmentally benignity, easily processability, reproducibility and manufacturability. To accomplish this, we strategically designed these hybrids by direct anchoring or physisorption of CoO and CO_3O_4 on two different variants of graphene: graphene oxide which is semiconducting, and its reduced form showing conducting behavior via mixing dispersions of the constituents under mild ultrasonication and drop-cast (or spray-cast) resulting in different combinations. This facile approach affords strong chemical/physical attachment and is expected to have coupling between the pseudocapacitive transition metal oxides and supercapacitive graphene showing enhanced surface activity/reactivity and reasonable areal density of tailored interfaces. We used a range of complementary tools to establish microscopic structure–property-function correlations including scanning electron microscopy combined with energy dispersive x-ray spectroscopy, atomic force microscopy, x-ray diffraction, transmission electron microscopy in conjunction with selected-area electron diffraction, and resonance Raman spectroscopy combined with elemental Raman mapping. They reveal surface morphology, local (lattice dynamical) and average structure and surface charge transfer/doping due to physically (or chemically) adsorbed cobalt oxide and highlight the surface structure and interfaces. This lays the groundwork to further investigate the electrochemical properties as high-performance supercapacitor cathodes, rechargeable secondary battery anodes and electrocatalytical platforms.

Key words: Graphene derivatives, cobalt oxides polymorphs, charge transfer, surface structure and tailored interface, Raman mapping, energy storage and conversion, electrocatalysis

INTRODUCTION

Graphene, a single atomic layer of sp^2-bonded carbon (sp^2 C) in which carbon atoms are bonded together in a hexagonal lattice resembling a honeycomb, has been hailed as the twenty-first century wonder material.[1,2] It has several superlative physical properties such as ambipolar electric field effect, high mobility of charge carriers ($\sim$20,000 $cm^2\ V^{-1}\ s^{-1}$), anomalous quantum Hall effect (QHE),[3] and massless relativistic carriers, all

(Received May 15, 2015; accepted August 26, 2015; published online September 10, 2015)

of which make graphene appropriate for many potential applications including graphene nanoribbon transistors, single molecule gas detectors, and transparent conducting electrodes. Moreover, field-effect transistors based on graphene are now considered a candidate for post-silicon and radio frequency electronics. It also exhibits a high theoretical specific surface area (2630 m^2 g^{-1})[4] and remarkable mechanical strength and flexibility (Young's modulus ~1 TPa)[5] suitable for supercapacitors (SCs)[6] and rechargeable secondary batteries (especially Li-ion) electrodes,[7] and advanced electrocatalytical[8] and nanobiocatalytical platforms.[9]

In addition to conventional graphene, the compound can be modified through a variety of chemical interactions via the presence of surface and edge functional groups and doping so as to form several graphene derivatives with tailored and desirable physical–chemical properties.[10] Graphene oxide (GO)[11] and reduced graphene oxide (rGO)[12] are some of the emerging graphene variants as novel functional nanoscaffolds in physical, chemical, electrochemical, electro- and bio-catalysis applications, including semiconducting materials in transistors,[13] liquid crystal devices,[14] hydrogen-based energy storage devices,[15] gas sensing,[16] electrochemical and biological sensors,[17] nanomedicine,[18] solar cells,[19] fuel cells,[20] and alternative renewable energy devices (supercapacitors[21,22] and rechargeable secondary batteries).[23] In fact, recently, GO has been emerging as a solution-processable material for large-area electronics because it can be readily and uniformly deposited on a range of substrates and reduced by various processing methods on a larger scale. While GO can be considered as insulating due to the presence of saturated sp^3-bonded carbon atoms bound to oxygen and a disordered analogue of the highly conductive crystalline graphene with oxygenated functional groups (i.e. –carboxyls or –COOH and epoxides or –ROOH at the edges and hydroxyls or –OH on the surface), its reduced form (rGO) containing residual (~2–8 at.%) oxygen and possibly amine groups from hydrazine monohydrate used for chemical reduction permits semiconductor transition and offers tunable electrical and mechanical conductivity over several orders of magnitude. The C–O bonds possess differing chemical reactivities based on the site or location and hybridization of the C–O bond, owing to the electron-withdrawing effect of sp-hybridized oxygen (carbonyl groups) and the donating effects of sp^2-hybridized oxygen (alcohol groups). In addition, the presence of a few sp^3 C sites disrupts the flow of charge carriers through sp^2 clusters so that the electrical transport in rGO occurs primarily by hopping rather than near ballistically,[24] as is the case for mechanically exfoliated classic monolayer graphene. However, it is noteworthy that the covalent oxygen functional groups give rise to remarkable mechanical strength[25,26] along with molecular-level chemical–biological sensing capability.[27–29] Moreover, these chemical modifications further tailor the surface chemistry to specific applications including hdyrodrophilic (GO) versus hydrophobic (rGO) that facilitates feasible interactions and surface and interface structure-dependent electrochemical and electrocatalytic activity. Alternatively, with these added advantages, it is desirable to harness the useful properties of graphene derivatives in hybrids and composites through the incorporation and directed assembly with various kinds of functional nanomaterials, including organic crystals, polymers, metal–organic frameworks (MOFs), biomaterials, carbon nanotubes (CNTs) and inorganic nanostructures.[29–31] It should be mentioned that, due to a lack of detailed knowledge on bonding configurations, location of the residual oxygen, density and type of defects generated during oxygen evolution, hybridization states of C–C and C=O bonds and their spatial distribution in Go and rGO, the nature of exact electronic structures is limited and is under intense exploration. Nevertheless, this limited knowledge and information does not prevent the research and development that facilitate facile surface structure and tailored interfaces for applied electrochemistry. There has been a large proliferation of portable consumer electronics and solar power, for which much effort has been devoted to lightweight, flexible, and even wearable electronics to meet the growing demands on electrical energy of the modern digital age.[32,33] In this work, we report on the preparation and properties of these functionalized graphene–inorganic hybrid materials.

The intermittent nature of sustainable energy sources (solar and wind energy) has ignited the demand for alternative energy storage materials and devices.[22] Electrochemical energy systems (supercapacitors, SCs, and rechargeable secondary batteries) represent efficient and environmentally friendly technologies.[34] In spite of the large energy density of batteries, they suffer from lower power density and shorter cycling life. In contrast, SCs offer longer life cycles and higher power density. Therefore, SCs are battery-complementary devices for high operating power level applications and they are emerging as critical components.[34] The energy storage mechanism in SCs is of two types: electrochemical double-layer capacitors (EDLCs) in which capacitance arises from charge accumulation in the electrode/electrolyte interface, and pseudocapacitors which are based on the fast and reversible redox reactions at the surface of electro-active materials.[35,36] In general, the capacitance of pseudocapacitors is higher than those of EDLCs. While a gamut of carbonaceous materials (activated carbon, AC; carbon nanotubes, CNTs; (meso)porous carbon, po-C; porous organic networks, PONs; activated graphene, AG; graphene and derivatives; graphene oxide, GO; and reduced graphene oxide, rGO) having higher specific surface area and elec-

trical conductivity dominate in the EDLCs,[37–42] the conducting polymers[43] and transition metal oxides (TMeO)[31] are commonly used for pseudocapacitors. The diverse and sustained success of carbons is due to structural polymorphism, chemical stability, wide operational potential window, relative inert electrochemistry, rich surface chemistry and electrocatalytic activities for a variety of redox reactions. Since SCs based on nanocarbons are performance-limited by themselves, novel functional materials with greater performance have become indispensable, and breakthroughs happen when new types of materials or new combinations of known materials with different dimensionality and functionality are designed. To address these issues, pseudocapacitive TMeO materials are being explored coupled with graphene and its derivatives. Among several redox-active materials (e.g. RuO_2, TiO_2, SnO_2, Mn_3O_4/MnO_2, NiO, V_2O_5, Fe_3O_4/Fe_2O_3, MoO_2 etc.),[31,44,45] recent research has evidenced that cobalt oxide polymorphs (i.e. CoO and Co_3O_4) appear to be quite promising with several advantages of being relatively cost-effective, with simple and scalable synthesis and processing, environmental benignity (harmful only by excessive inhalation), higher specific capacitance, wide operational potential windows and stability through multiple cycling and rich electrochemical properties, such as rapid charging–discharging (multiple cycling) available with various metal oxidation states (Co^{2+}/Co^{3+}).[30,46]

The cobaltous oxide or cobalt monoxide, CoO, crystallizes in the periclase (rock salt) crystal structure consisting of two interpenetrating fcc sublattices of Co^{2+} and O^{2-} with space group $Fm\bar{3}m$. These two sublattices are shifted along the body diagonal by half its length, and thus each ion has six of the other ions as its nearest neighbors with alternate oxide and metal ion centers, but shows a wide range of stoichiometry.[47] The other polymorph, Co_3O_4, is a unique mixed valence compound with its formula sometimes written as $Co^{2+}Co_2^{3+}O_4$ and sometimes as $CoO.Co_2O_3$, which adopts the normal cubic spinel structure having space group $Fd3m$, with Co^{2+} ions in tetrahedral interstices and Co^{3+} ions in the octahedral interstices of the cubic close-packed lattice of oxide anions at ambient conditions.[48,49] Despite simple stoichiometry of Co:O = 3:4, it is considerably more complicated than CoO = 1:1. It is worth mentioning that there is Co_2O_3, which is a metastable form and if it exists it acquires a hcp hexagonal structure with lattice parameters a = 4.640 Å and c = 5.750 Å. Therefore, in parallel, CoO and Co_3O_4 are considered the most promising candidates for applied electrochemistry.

Graphene-based hybrid materials have opened up new frontiers in science and technology and have expanded the scope of graphenes, since synergistic effects can result from the interaction between graphene and TMeO nanomaterials supported onto/into graphene.[31,50,51] In hybrid systems, the constituents

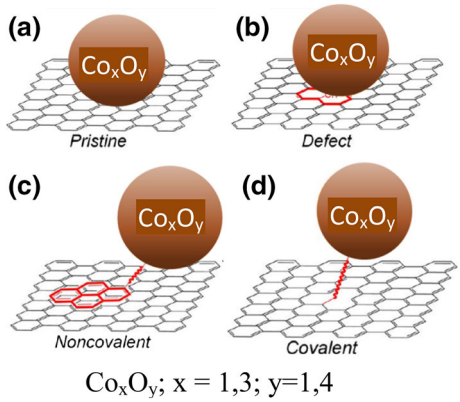

Fig. 1. (Color online). Schematic illustrations of different types of transition metal oxide nanoparticle (TMeONP)–graphitic interfaces. (a) The pristine interface where TMeONP and graphitic surfaces are in direct contact; (b) TMeONP – defect interface where atoms of TMeONP are bonded to the defect sites of the graphitic surfaces; (c) noncovalent interface or physisorption where functional moieties of graphitic surfaces interact through noncovalent interactions with TMeONP; (d) covalent interface where covalent bonding or chemisorption between graphitic surface and its functional moieties and TMeONPs is formed.

are usually bound by some interaction, for example, strong covalent-like,[52] or weak, as in some layered materials intercalated with polymers.[53] Figure 1 illustrates a range of possible TMeO nanoparticle (TMeONP)–graphitic interfaces that can be formed either separately or concurrently. The concept of the hybrid system extends to situations in which, despite the absence of a physical bond between the components, they can influence each other via tailored interfaces affecting novel functions, which is the case here.[54] This broad definition of hybrids encompasses systems whose properties are governed by proximity effects, for example, proximity-induced superconductivity and anomalous magnetic effects. In sp^2-bonded carbons (sp^2 C), interface atoms are a strong, if not the main, fraction of the hybrids, which is an attractive feature for engineering properties.[55] Graphene-based hybrids are prepared following chemical routes, where GO and rGO can serve as both a supporter and a conduction channel for shuttling electrons involved in redox reactions during electrochemical processes, which is the case here. Despite substantial research activity, the insights into establishing structure–property relationships from the viewpoint of surface and/or local charge transfer and interfacial aspects are limited. n- and p-type doping of graphene achieved through surface transfer doping or traditional substitutional doping and their electronic applications are of great importance.[56] Recently, metal adatoms and clusters on graphene have been a topic of great interest and it is expected that they locally dope or modify the band structure.[57–59] Additionally, different morphologies arising due to the multi-faceted crystallite structure

of metal oxides have a direct bearing on electrochemical and electrocatalytic oxygen reduction reaction activities. We aimed to develop hybrid nanomaterials by utilizing GO and rGO (supercapacitive) coupled with CoO and Co_3O_4 (pseudocapacitive)[60] for applied electrochemistry. We strongly believe that graphene–inorganic interfaces can offer additional electrolyte-transport paths for electron transfer and proton/cation diffusion due to the unique micro-spherical architecture constructed from smaller nanoparticles. They are investigated in terms of structure and physical properties highlighting the surface structure and interfaces from the point of view of exploring and identifying the nature of charged defects, laying the groundwork for energy storage and conversion devices as advanced electroanalytical (electrochemical and electrocatalytical) platforms.

EXPERIMENTAL METHODS

Sample Preparation

To synthesize thin films of GO, rGO and their hybrids with polymorphs of cobalt oxides (CoO, Co_3O_4) nanopowders, 10-mL dispersions of 0.085 mg/mL of GO (and rGO), 0.1 mg/mL of CoO and Co_3O_4 were prepared in DI (Milli-Q) water. GO was prepared via a modified Hummer's method followed by chemical reduction using hydrazine monohydrate.[61–63] We stirred each of these solutions mildly for around 1 h at room temperature followed by ultrasonication for around 40 min. Each graphene-based material dispersion was individually combined/mixed with each cobalt oxide in a 3:1 ratio by volume-forming hybrid solutions used in this study to determine an optimized configuration via mild ultrasonicated for 30 min. The thin films from each of these mixed dispersions were made by drop-casting and were air-dried on commercial Si(001) substrates coated with 285 nm of SiO_2 of approximately 1 cm^2. This approach affords strong physisorption leading to enhanced electrochemical and electrocatalytical activity/reactivity. A complete listing of the materials with reference sample ID number (S1–S8) is summarized in Table I.

Sample Characterization

Scanning electron microscopy (SEM) images were taken with an instrument (Model JEOL 5400LV; MA, USA) operating at primary electron acceleration voltage (V_{acc}) of 10 kV and at constant current of 45 μA in secondary electron imaging (SEI) mode, collected by an in-lens detector equipped with an x-ray ISIS EDS (energy dispersive spectroscopy) system providing surface topography. We also used BEI mode for EDS measurements yielding elemental composition contrast. Atomic force microscopy (AFM) was performed in non-contact modes in ambient condition using a PicoPlus instrument series 5500 (Molecular Imaging, MI, USA). The AFM tips were of silicon with nominal resonance frequency and spring constant of 15 kHz and 0.2 N/m, respectively, and the scan speed varied depending on the image size and ranged from 1 μm/s to 10 μm/s, lateral optical level sensitivity of $\leq$1 μV and manufacturer's stated tip radius of curvature when first used of $<$10 nm (BudgetSensors, ContAl, Bulgaria). Samples for TEM and SAED were prepared by placing one to two drops of the individual component and of the hybrids on commercial lacey carbon Cu grids (Ted Pella, CA, USA) and allowing it to air-dry giving several regions and sufficient numbers of isolated flakes and particles. TEM images and selected area electron diffraction (SAED) patterns were taken using a JEOL 1400Plus operating in cryo-EM, energy dispersive x-ray analysis, SAED and tomography modes at 100 kV and 1 nA with a JEOL Be specimen holder, a Gresham SiLi detector with Moxtek AP3.3 window (allowing elemental detection down to boron), and an IXRF Systems control software and hardware. For SAED, we used a 0.23-μm aperture, with a small spot size and spread beam to increase the

Table I. Summary of graphene oxide (GO) and reduced graphene oxide (rGO) and their hybrids with nano-/micro-cobalt oxides i.e. CoO[Co(II)] and Co_3O_4[Co(II, III)]) prepared using mild ultrasonication followed by drop-casting and drying at room temperature

Saample ID	Sample material specification
S1	GO (oxidized form of graphene with functional moities attachment at edge and basal plane)
S2	rGO (reduced form of graphene oxide or quasi-graphene)
S3	CoO (Cobalt(II) mono oxide); Periclase (rock salt) crystal $Fm\bar{3}m$ structure with Space group, O_h^5
S4	Co_3O_4 (Cobaltosic(II, III)); Spinel crystal structure with space group, O_h^7; Co^{2+} ions occupy the tetrahedral (or A) sites and Co^{3+} ions the octahedral (or B) sites
S5	S1 + S3 (drop-cast on SiO_2/Si wafers and air-dried at RT)
S6	S1 + S4 (drop-cast on SiO_2/Si wafers and air-dried at RT)
S7	S2 + S3 (drop-cast on SiO_2/Si wafers and air-dried at RT)
S8	S2 + S4 (drop-cast on SiO_2/Si wafers and air-dried at RT)

electron coherence length at the sample. For electron tomography, single axis tilt-series were collected and processed using "SerialEM" IMOD and eTomo software (developed by the University of Colorado-Boulder, USA). The tomography software is fully integrated with an 8-M pixel AMT bottom-mounted digital camera. TEM measurements provided nanoscale morphology and structure that help to determine interplanar spacing and tomography for capturing interfaces. Allowing more detail and a greater understanding of the interaction between graphene derivatives and cobalt oxides, we also measured average and local crystal structure. X-ray diffraction (XRD) was obtained with Siemens Model D2000 instrument (now Thermo Scientific, MA, USA) and the x-ray diffractograms were acquired in Bragg–Brentano geometry ranging 2θ from 8° to 70° using Cu K_α (λ = 1.5405 Å) x-ray source operating at voltage of 45 kV and current 40 mA. Samples were run at a scan rate of 0.04°/s or, to improve signal-to-noise ratio, we also measured at a scan rate of 0.02°/s. Raman spectra of all samples were measured to determine the lattice vibration at various areas of interest on the nanostructure hybrid surfaces. The Raman spectra were recorded using a micro-Raman spectrometer (Model InVia; Renishaw, UK) equipped with excitation laser of wavelength 633 nm (E_L = 1.92 eV) and ~4–6 mW incident at the sample, with edge filters cutting at ~100 cm^{-1}. The scattered light from the sample was collected in backscattering geometry, transmitted by a beam splitter and detected by a CCD camera. An objective lens of ×50 was used providing spot size of 2 μm. Extreme care was taken to avoid sample damage or laser-induced thermal degradation. The reflected light was filtered using an edge filter to remove the laser excitation and then sent to a spectrometer. Raman shift was ranged from 200 cm^{-1} to 3200 cm^{-1} for Co-containing hybrids, while for GO and rGO, it was kept between 1150 and 3200 cm^{-1} with spectral resolution of 1 cm^{-1}. The acquisition time per pixel was a few minutes to slightly less than an hour for Raman mapping with spatial resolution of 0.15 μm (150 nm) or 0.10 μm (100 nm) in an area of 20 × 20 μm^2. For room temperature electrical property, we made electrical contacts with colloidal silver paste and attached a Cu wire for connection. We measured two-point contact resistance with a Keithley 2400 source meter (Keithley, OH, USA) and determined room temperature dc electrical conductivity (σ_{dc}) for all the samples.

RESULTS AND DISCUSSION

The effective characterization of metal oxide–graphitic interfaces is rather challenging as compared with the straightforward overall hybrid morphology. The interactions at the interfaces play essential roles in the synthesis (morphology and structural control), properties (physical), and applications (materials' performance). Therefore, understanding the interface is urgently needed for promoting the development of advanced graphene-based hybrid material systems.[64] Figure 2 shows SEM micrographs at various length scales of constituents (GO, rGO, CoO and Co_3O_4) and of hybrids (CoO/GO, CoO/rGO, Co_3O_4/GO and Co_3O_4/rGO), revealing distinct surface morphology evolution, particle size and type variation (radiated spherulite versus spherical), number of graphene oxide nanowalls through thickness contrast and crumpled/wrinkled sheets, rGO flakes size distribution and homogeneity/uniformity of densely packed thin films. The numerous aggregated nanoparticles with different shapes can be seen observed and their diameter varies between 20 and 100 nm. Figure 2 also shows well-faceted crystallites of Co_2O_3 polymorph for morphological comparison with other cobalt oxide polymorphs. We have measured BEI images (not shown) and EDS of CoO/GO and Co_3O_4/GO revealing elemental composition (gray, low Z C and O versus dark, high Z Co) the analysis of which confirmed that the crystals are made of C, Co and O with a chemical formula of Co_3O_4, including 80% Co_3O_4 and 20% CoO, which is in agreement with a partially mixed system verified by XRD, as discussed below. Moreover, we determined the Co/C ratio, which turned out to be 0.78 at.% and 0.02 at.%, respectively. This implies that for every carbon element there is 0.0078 Co and 0.004 Co in CoO/GO and Co_3O_4/GO hybrids, respectively. The surface morphology at nanoscale was determined using TEM as shown in Fig. 3 at different magnifications along with SAED ring/spots and intensity patterns. Graphene ring intensity patterns are included as a reference and most of the peaks of hybrids show graphene and graphene oxide peaks at 1.06 Å, 1.23 Å, 1.71 Å, 2.12 Å and 4.41 Å.[2] From the TEM images, the crystalline defects such as stacking faults and dislocations are not apparent, and from the nanoscale surface morphology it is apparent that the metal oxide nanoparticles are laid upon the nanosheets/nanowalls/nanoedge/nanofolds of GO and rGO. The SAED pattern reveals the quasi-single crystalline nature of Co oxides with rock salt and spinel structure that are indexed suitably in agreement with the XRD discussed below. Figure 3 also shows the general morphology of the as-prepared CoO_x nanoparticles consisting of intertwined aggregates and occasionally Co_3O_4 as nanoctahedron-shaped crystallites containing two inverted pyramids attached at their square base and ounded by eight triangular facets, unlike CoO which is rather either spherical or cube-shaped. Moreover, these images show well-dispersed nanoparticulates anchored on the graphene sheets/flakes/nanowalls. An enlarged TEM image shows lattice fringes with interplanar spacing d of 0.392 nm and 0.80 nm, corresponding to the (311) planes of Co_3O_4 crystals and 0.279 nm, which is equal to the lattice constant of the {400} plane of Co_3O_4. On the other hand, the well-resolved lattice fringes/rings in SAED give an

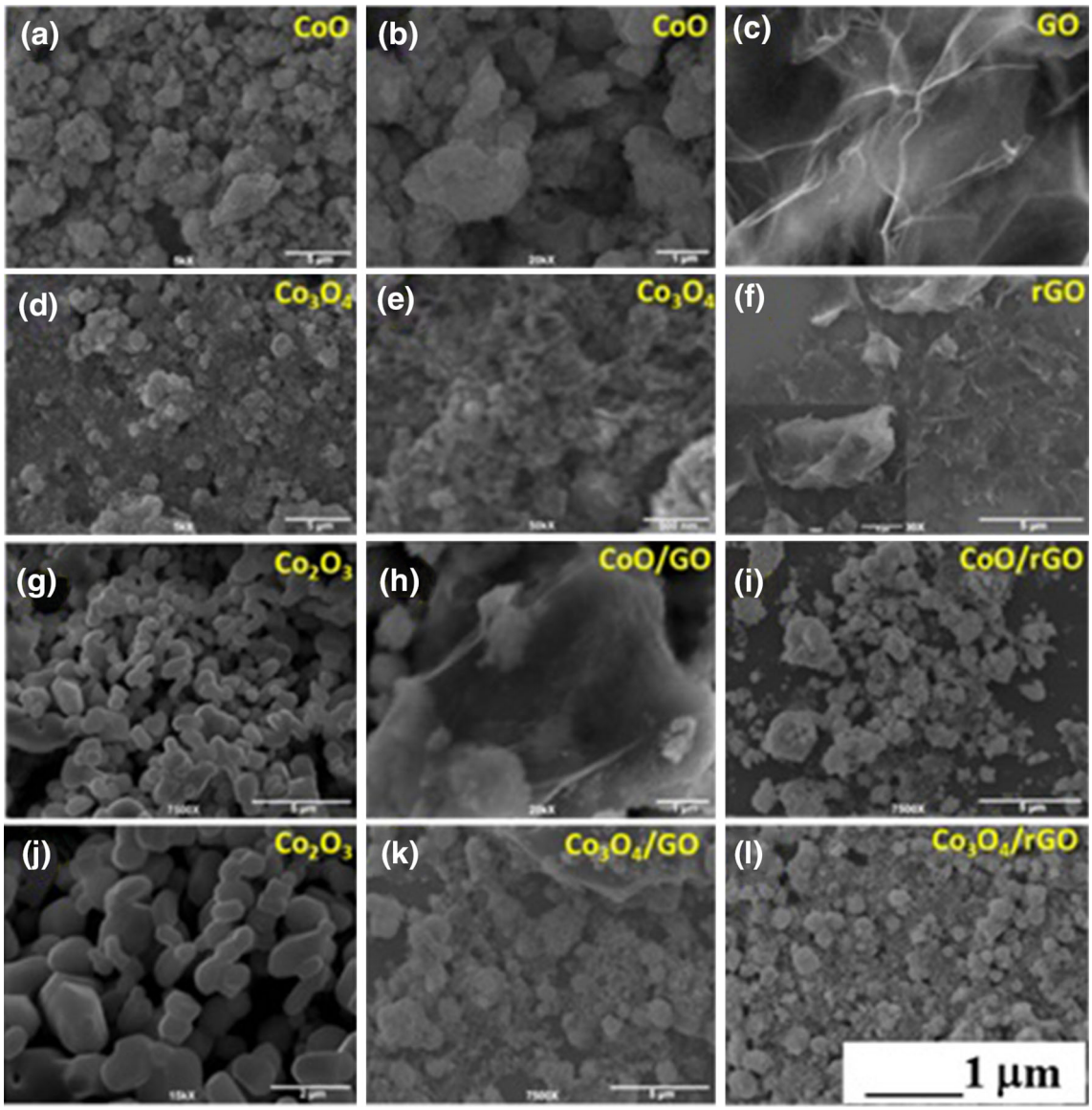

Fig. 2. (Color online). Scanning electron microscopy (SEM) images of nano-/microscale cobalt oxides (a, b) CoO [Co(II)] (c) graphene oxide (GO) (d, e) Co_3O_4 [Co(II, III)]) (f) reduced graphene oxide (rGO) (g, j) Co_2O_3 and their hybrids (h) CoO/GO (i) CoO/rGO (k) Co_3O_4/GO and (l) Co_3O_4/rGO measured with 10 kV in secondary electron imaging (SEI) mode with constant current of ~45 μA. (Scale bars are shown at the bottom of the images).

interplanar spacing of 0.45 nm, 0.246 nm and 0.213 nm, in good agreement with the distance of the (111) (200) and (220) planes for CoO. Overall, in most of these patterns, there is a dominant crystal phase with random orientation, which seems to have fcc-type rings (space group, $Fm\bar{3}m$).[65,66] An attempt was made to image the graphene–cobalt oxide interface using electron tomography (see Fig. 3 which displays representative Co_3O_4/GO and CoO/GO hybrids) exhibiting the physical adsorption in three-dimensional TEM image and reconstructed images using ImageJ software. The AFM images in two- and three-dimensions in 5 × 5 μm^2 area show surface topography, provided in Fig. 4a and b for (CoO and Co_3O_4)/GO and (CoO_2 and Co_3O_4)/rGO, respectively. The corresponding analyses in terms of grain size (d) and root mean square surface roughness (σ_{rms}) is summarized in Fig. 5. It is apparent that there is a marginal change in σ_{rms} (10 nm → 24 nm) and an increase in d (8 nm → 50 nm) with the presence of cobalt oxides on rGO and GO nanosheets. The AFM results provided an estimate of cobalt oxide nanoparticulates size albeit locally averaged to 50 nm and 160 nm for CoO and Co_3O_4, respectively. As anticipated, the thickness difference determined through line scan using Gwyddion software between each layer of GO and rGO is ~0.485 nm, which is marginally higher than anticipated (0.34 nm).[67] X-ray diffraction (XRD) has been used to determine the crystallinity and structural phases in various forms as well as determining lattice spacing (d_{hkl}) and crystallite or grain size

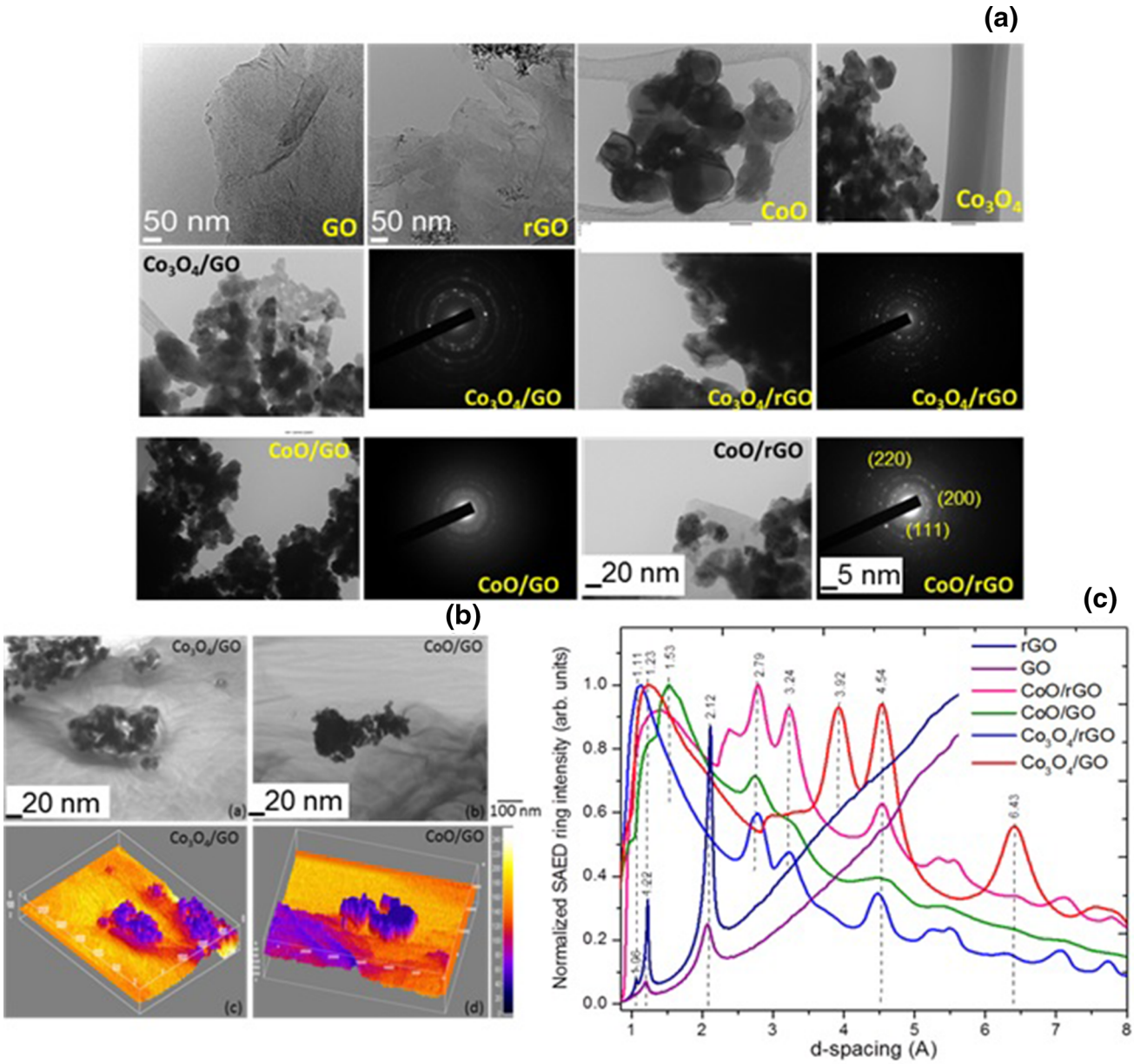

Fig. 3. (Color online). Transmission electron microscopy (TEM) images taken with 200 kV besides selected-area electron diffraction (SAED) with an aperture size of 200 nm for (a) CoO/GO, CoO/rGO, Co_3O_4/GO and Co_3O_4/rGO. The morphology exhibiting surface modulations and corrugated structures with small and big wrinkles is consistent with all kinds of microscopy techniques *albeit* in different spatial length scales. For SAED, condensate aperture 0.20 μm in Köhler condition with a small spot size was used to obtain a small, practically parallel beam with an illumination angle of 0.16 mrad and an area of 200 nm in diameter and beam was spread to increase the electron coherence length at the sample. The electron diffraction data were recorded on CCD for further quantitative analysis. GO/rGO rings and diffraction spots of CoO and Co_3O_4 are apparent. (b) The electron tomography three-dimensional images for two of the representative samples are shown as example. (c) The corresponding real space (d_{hkil}) intensity pattern revealing crystal structure of 'hybrids' is also provided (Scale bars are shown at the bottom of the images).

(L_{hkl}). Figure 6 shows the XRD diffractograms of the constituents (graphene derivatives and cobalt oxides) and of the graphene-based hybrids. The XRD pattern of GO is dominated by a single broad peak at 2θ = 16.6° (002) corresponding to an interlayer distance of 0.74 nm (Fig. 6, top left). Alternatively, it shows larger interplanar spacing than that of graphene, attributed to the lattice expansion consistent with oxidation of the graphene sheets, intercalation of water molecules and other functional moieties held in the interlayer galleries of hydrophilic GO. On the other hand, the pattern of the hydrazine-reduced rGO contains a very broad reflection at 24.5° (002) corresponding to interplanar spacing d of 0.36 nm, which can be indexed to disorderedly stacked or restacked graphene nanosheets, and a peak at ~12° which corresponds to a *c*-axis spacing of 0.69 nm. This is in addition to the peak at 16.6° similar to GO which is ascribed to the residual carboxyls and hydroxyls groups in rGO, presumably induced by a bimodal or multimodal character of the interplanar spacing of rGO. Al-

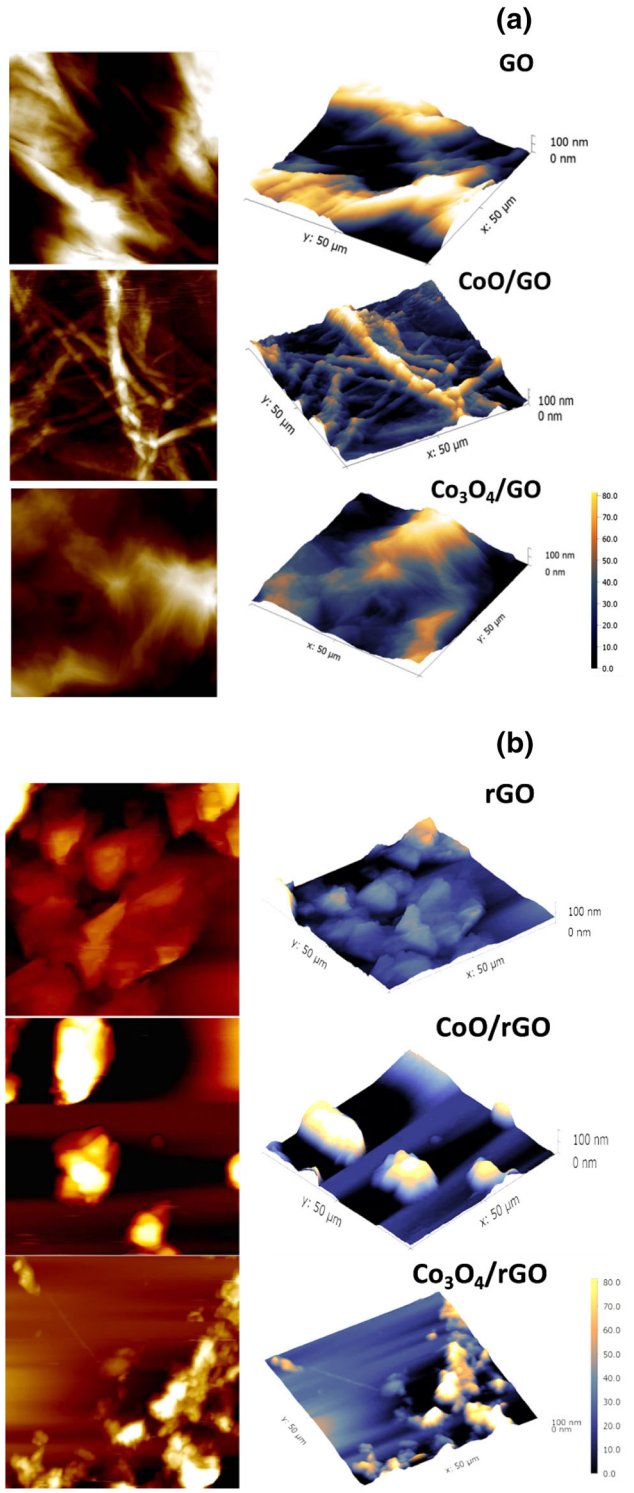

Fig. 4. (Color online). Atomic force microscopy (AFM) in contact mode showing surface topography along with three-dimensional representation obtained using Gwyddion software for representative set of (a) graphene oxide (GO) and (b) reduced graphene oxide (rGO) hybrids with nano-/micro-cobalt oxides i.e. CoO [Co(II)] and Co_3O_4 [Co(II, III)]), in 5 × 5 μm^2 area.

though the reduction mechanism of rGO is not yet claimed, it appears that the reduction starts from the edges of GO sheets (relatively more energetic) and proceeds into the basal planes. During the reduction, parts of the basal planes near the edges become reduced and subsequently snap together due to π–π^* interactions, thus narrowing the interlayer distance. Consequently, the reducing agent, monohydrate hydrazine, cannot penetrate further into the interior of the rGO particles, presumably leading to the lower degree of reduction, which corresponds to *c*-axis spacing of 6.91 Å. All the XRD peaks (CoO and Co_3O_4; Fig. 6, bottom left) can be indexed with cubic spinel-type Co_3O_4 (JCPDS card No. 78-1970 and JCPDS card no. 43-1003, a = 8.08 Å) phase and rock salt periclase CoO (JCPDS card No. 15-0806) phase including (111), (200), (220), (222), (311), (400), (422), (440), and (511). The insets in Fig. 6 show schematics of the unit cell structures for both the cobalt oxide polymorphs. No characteristic peaks from other impurities are detected. The Rietveld refinement procedure was performed for the investigation of the crystalline structure of as-prepared nano-/micro-crystallites films of CoO and Co_3O_4. It can be shown that some of the peaks at 2θ = 31.29°, 36.81°, 59.37°, and 65.27° are correspondingly indexed to the (220), (311), (440) and (511) reflections of the periclase CoO and of the spinel-type Co_3O_4. The peaks are sharper, indicative of their better crystallinity with lattice constant of $a = b = c$ = 8.02 Å and $a = b$=4.258 Å based on (220), (311) and (400) planes.[68] The crystallite size is obtained from XRD analysis using the Debye–Scherrer equation following the relationship: $L_{hkl} = K\lambda/\beta_{hkl} \cos \theta_{hkl}$, where L_{hkl} is the crystallite size in nm, λ is the wavelength of Cu K_α, β_{hkl} is the full-width at half-maximum and K = 0.94 is the shape or structure constant. The diffraction peaks of hybrids are broad and of low intensity while preserving phases of the components' implication of forming truly high-quality hybrid composites. The peak at 2θ = 31.29° is used to determine the lattice spacing (d_{hkl}) and particle size (L_{220}) of hybrids, the analyses of which are shown in Fig. 7a and b, respectively. An increase in lattice spacing (4.8 → 9.0 Å) and particle size (2.8 → 3.6 nm) of the hybrids is apparent as compared with rGO and GO. The crystallites size increase can be understood by considering the merging process induced by the functional groups of graphene derivatives, as well as the dangling bonds related to the cobalt oxides which are associated with the cobalt and oxygen defects at the grain boundaries and surface of the nanoparticles. As a result, these defects are favorable to the linking process, resulting in the larger grain or crystallite values. It is also important to

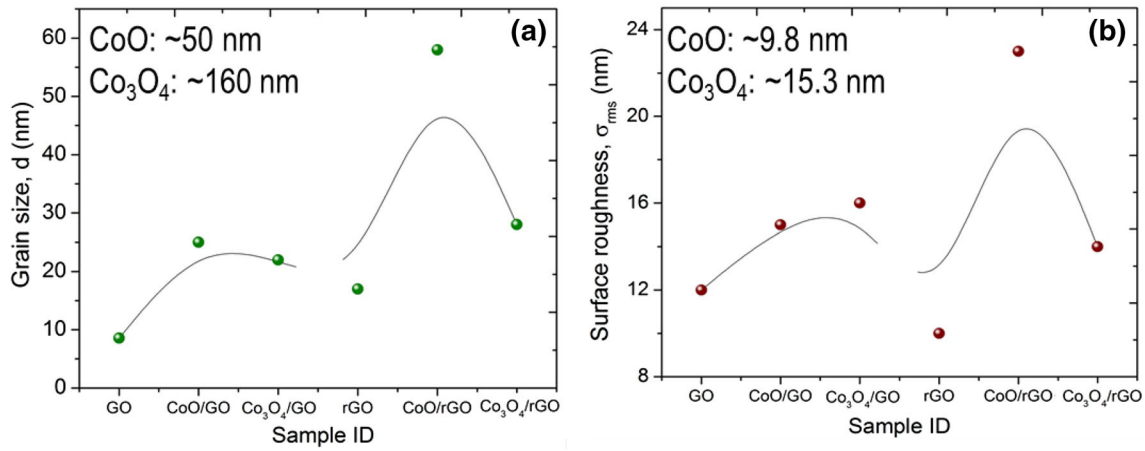

Fig. 5. (Color online). Variation of (a) grain size (d, nm) and (b) surface roughness (σ_{rms}, nm) deduced from AFM shown in Fig. 4 for all of the samples along with individual components.

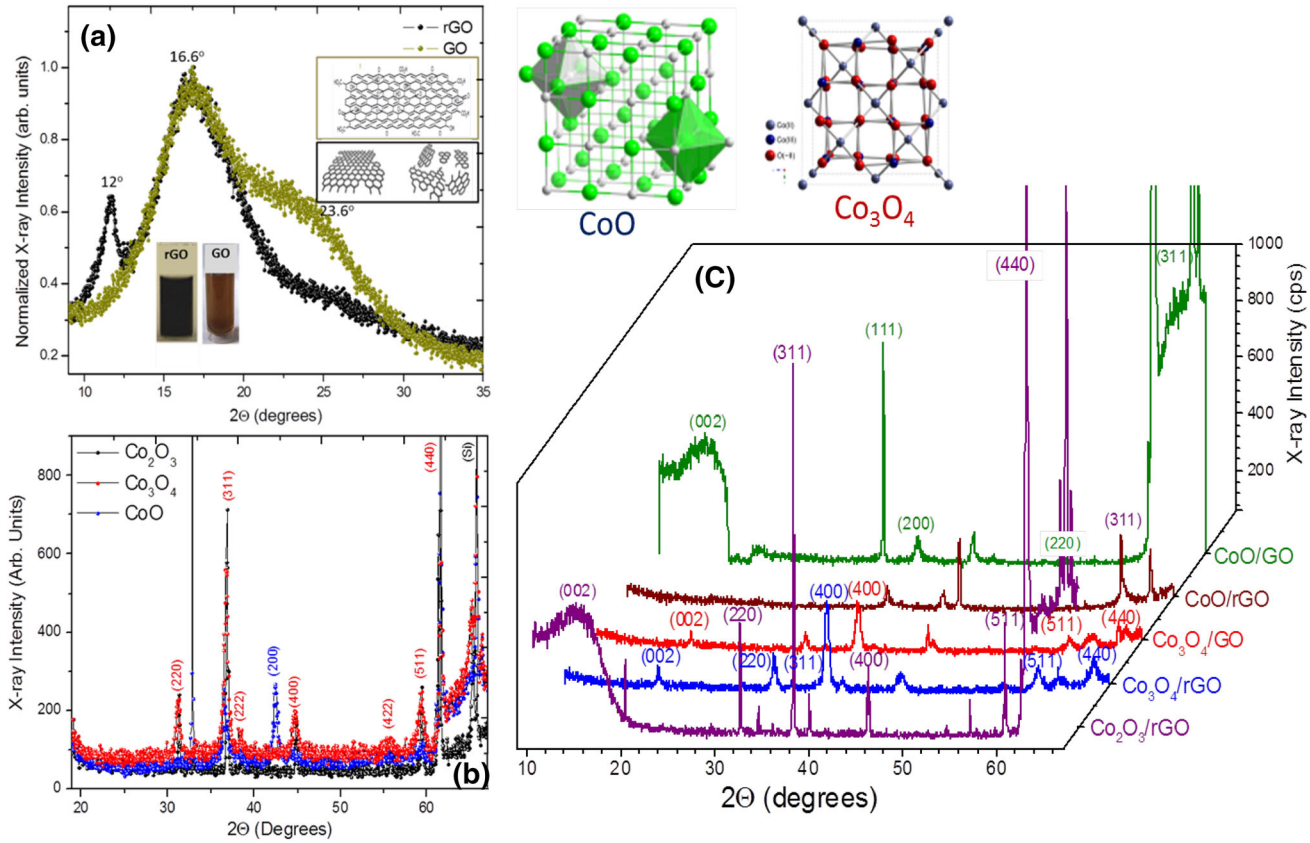

Fig. 6. (Color online). XRD diffractograms for (a) graphene oxide (GO) and reduced graphene oxide (rGO); (b) nano-/microscale cobalt oxides i.e. CoO [Co(II)] and Co_3O_4 [Co(II, III)]), and (c, d) their hybrids showing characteristic peaks in various regions. The peaks of interest for hybrids are marked with their (hkl) index. All of the diffractograms are taken in θ–2θ geometry with Cu K_α x-ray source (λ = 1.5405 Å). The unit cell for both CoO and Co_3O_4 is also shown.

note that the XRD determines the size variation of the coherent diffracting domain (CDD), since they are smaller than the actual particle sizes, which is the case here. *Raman spectra of free CoO and Co_3O_4*: Raman spectroscopy (RS) in general is a sensitive technique for crystallization, local structural disorder and defects in materials, and it is used to gain information about the structure of the precursor phases (Fig. 8a and c) and the graphene sheets in the hybrid composites (Fig. 8b, d, and e). RS of graphene-based systems is rather well documented,[69] and briefly of various cobalt oxides;[70–72]

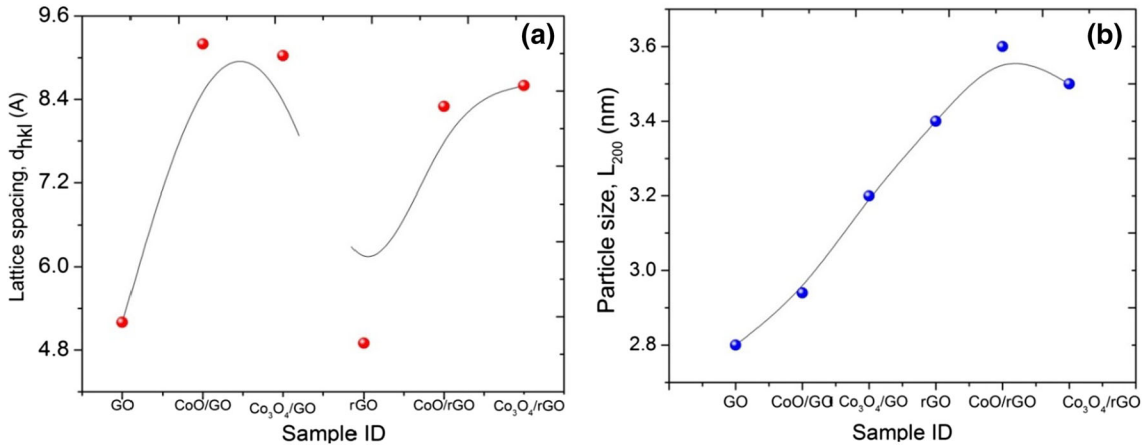

Fig. 7. (Color online). Variation of (a) lattice spacing (d_{hkl}, Å) from Bragg's law and (b) particle size (L_{200}, nm) determined from Debye–Scherrer formula for all of the samples along with individual components. The corresponding lattice constants (*a*, *b* and *c*) for bulk CoO [Co(II)] and Co_3O_4 [Co(II, III)]) are also shown as legends.

however, not of graphene-supported hybrids of cobalt oxides. Here, we attempt to investigate the possibilities of characterizing these promising graphene-supported cobalt oxides nanomaterials as electrochemical electrodes. This is keeping in view of the local distribution of oxygen-bonded species on the graphene support and its evolution with increasing amounts of different cobalt oxide polymorphs. Under the Raman microscope, the laser beam was focused on the surface of thenanoparticulates and/or thin crystallites and it was noted that there was minimal dependence of excitation laser wavelengths used on the spectra of free cobalt oxides. The micro-Raman spectra of free Co_3O_4 and CoO micro-/nanoparticles consist of five characteristic Raman-active peaks at ~194.4 (F_{2g}; LO), 482.4 (E_g; TO), 522 (F_{2g}; LO),618.4 (F_{2g}; TO)and 691.3 (A_{1g}; TO) cm^{-1} corresponding to skeletal vibrations, which are in good agreement with the bulk cubic CoO and Co_3O_4 phases reported in the lietrature.[70,73] The bands are sharper for both the CoO and Co_3O_4 (full-width at half maximum of 4.9, 6.0, 9.5, 7.3, 6.9 cm^{-1}), while marginally broader and shifted for Co_2O_3 which may be due to the bonding character. The spectra are shown for comparison, since Co_3O_4 is equivalent of $CoO.Co_2O_3$, consisting of both the CoO and Co_2O_3 phases. Based on irreducible representations for Co_3o_4, which crystallizes in the normal spinel structure $Co^{2+}(Co^{3+})_2O_4$ (space group O_h^7) with $Co^{2+}$and Co^{3+} occupying tetrahedral and octahedral sites, respectively, the reduction of the 42-dimensional representation of the vibrational modes at $k = 0$ (zone center phonons) into irreducible representations of the factor group O_h^7 gives: $\Gamma = A_{1g} + E_g + 3F_{2g} + 5F_{1u} + 2A_{2u} + 2E_u + 2F_{2u}$. The A_{1g}, E_g and three F_{2g}modes are Raman active. Of the five F_{1u}modes, four are infrared active and one is an acoustic mode. The remaining $2A_{2u}$, $2E_{2u}$, and $2F_{2u}$ modes are inactive. The assignment of the phonon symmetries of optically active vibrations (both longitudinal, LO; and transverse, TO) is based on the results of factor-group analysis of the lattice vibrations of the spinel structure mentioned above. Simple calculations for back scattering from the (111) surface show that the scattering cross-section should not depend on the rotation of the crystal surface around the propagation direction of the incident light.[73] Moreover, the TO–LO splitting supplies a criterion for the ionic character. The high-frequency peak, A_{1g} at ~692 cm^{-1}, has been assigned to a vibration that is largely determined by the octahedral cations in the normal spinel, whereas $F_{2g} \sim 522$ cm^{-1} and E_g modes combine the vibrations of tetrahedral and octahedral sites. Furthermore, this was attributed to Co–O lattice vibrations in CoO or corresponding to distortion vibration of Co–O in an octahedral environment in Co_3O_4. Among the signals of the CoO Raman spectrum shown in Fig. 8b and e, the strongest bands lie at 190 cm^{-1}, 482 cm^{-1}, and 691 cm^{-1}; the latter may be assigned to Co formed during the spectrum acquisition because of the local heating of the samples. However, all the samples seem quite thermally stable since no extra bands appear or they showed no variation in their band position due to local laser heating. The intensity recorded for the band at 691 cm^{-1} is, however, much larger for CoO compared with the band in Co_3O_4 film. The appearance of a 427-cm^{-1} band in the case of CoO excited with a 10-mW laser power is explained by the formation of a new compound which was identified as metastable Co_2O_3 with a distorted periclase structure, an intermediate formed during the decomposition of CoO to Co_3O_4 or vice versa. Therefore, the peaks at ca. 427 cm^{-1} and 180 cm^{-1} can be considered as the characteristic features of CoO. Knowing that, as regards to the oxidation state of the cobalt ions, Co_2O_3 is nearer to Co_3O_4 than CoO, one can understand why Co_2O_3 decomposed and the features of Co_3O_4 are pronounced in its Raman spec-

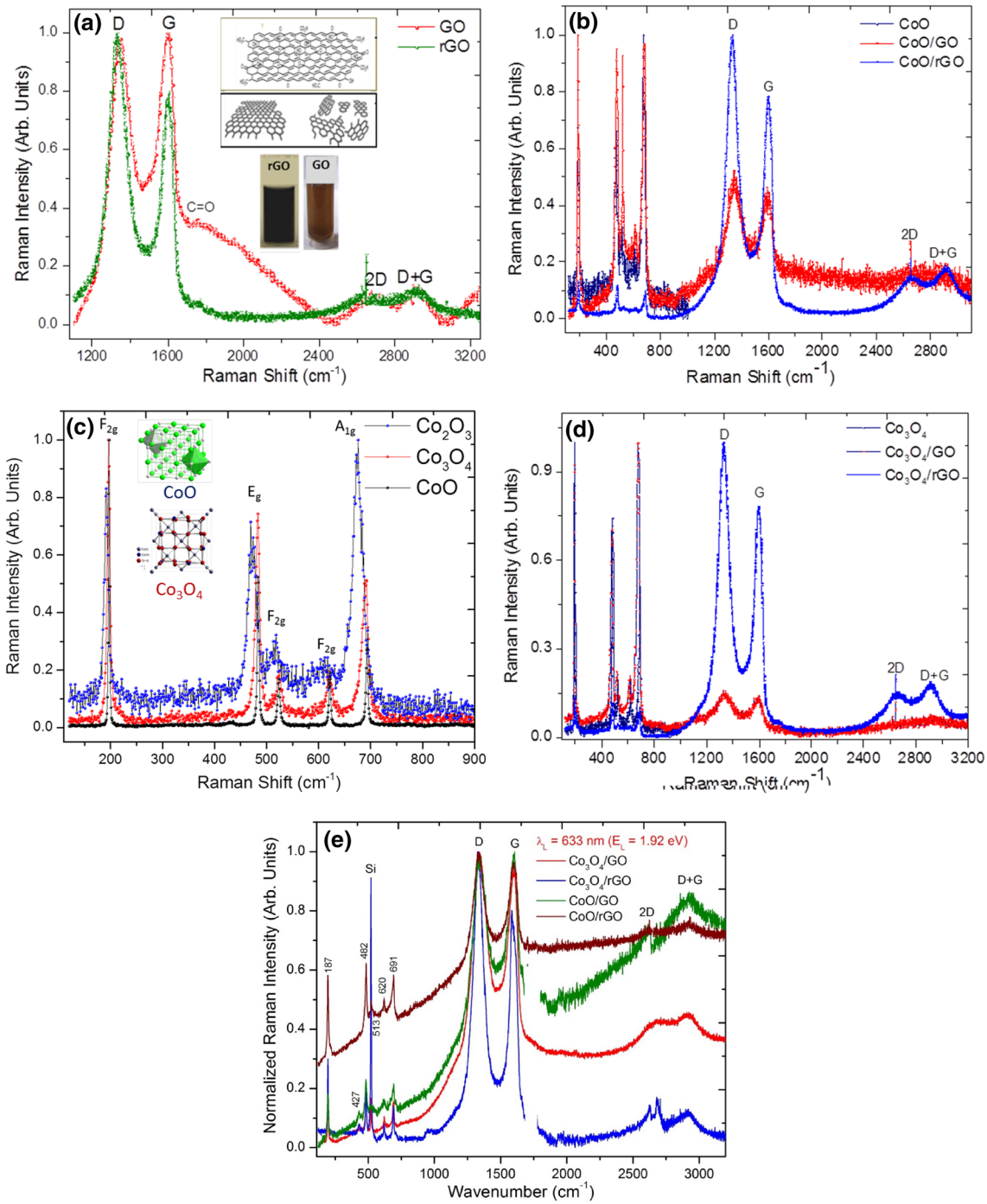

Fig. 8. (Color online). Representative micro-Raman spectra excited at 633 nm wavelength (E_L = 1.92 eV) showing characteristic peaks for GO and rGO hybrids with nano-/microscale cobalt oxides (b, e) CoO [Co(II)] and (d, e) Co_3O_4 [Co(II, III)]), in 150–3200 cm^{-1} spectral window along with constituents (a, c).

trum. Curiously, there is no similarity between our Co spectrum and that of Ref. 72 except for some differences between the relative peak heights and Co having the same feature as CoO. For symmetry considerations, while the scattering for all Raman modes was rather strong, particularly for the 690 cm^{-1} mode, which is assigned as A_{1g} mode, this is attributed to the stretching mode of Co–O bond in CoO_6 octahedra, because the structural framework of cobalt oxides consist of CoO_6 octahedral units shared by corners and/or edges similar to manganese oxides.[74,75] It is worth mentioning that, in CoO, Raman scattering comes from a collective vibration mode of the CoO_6 octahedron. The peaks

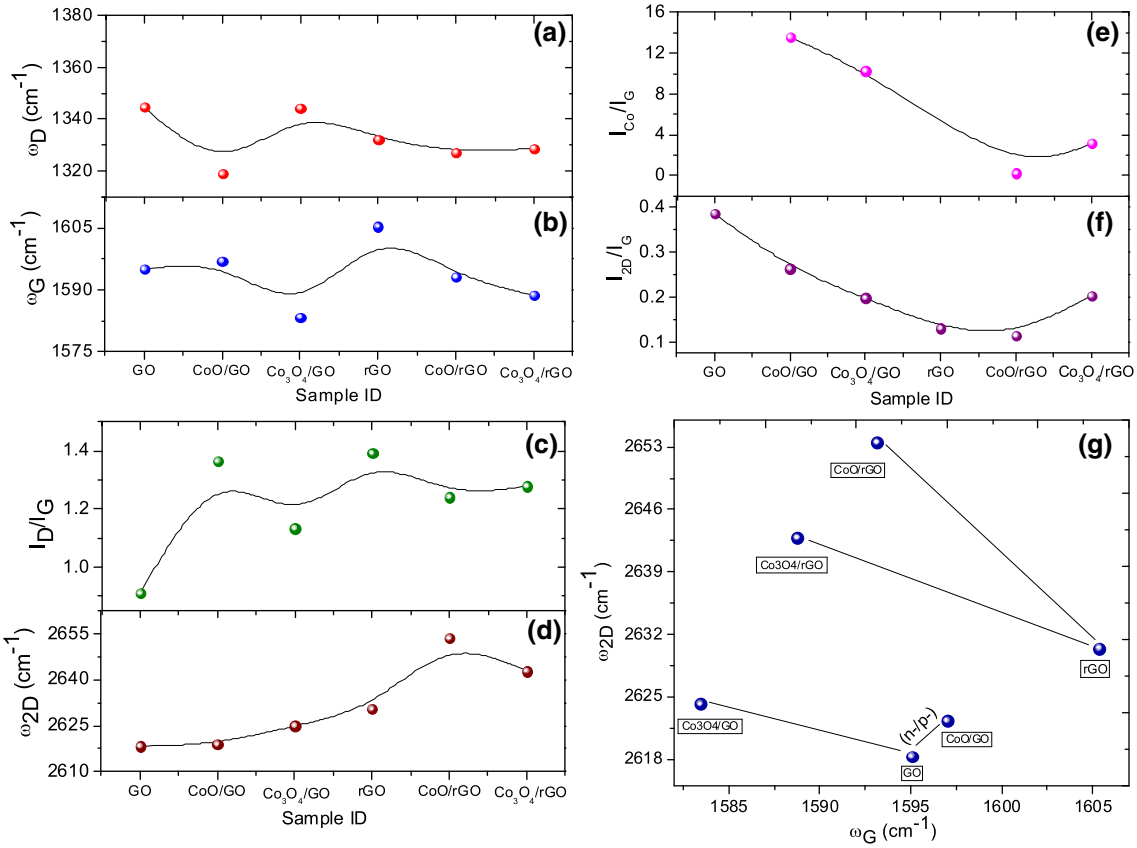

Fig. 9. (Color online). Variation of prominent Raman spectral bands for GO and rGO hybrids with nano-/microscale cobalt oxides: CoO [Co(II)] and Co_3O_4 [Co(II, III)]), in terms of (a) D band position (ω_D), (b) G band position (ω_G), (c) intensity ratio of D to G band (I_D/I_G), (d) 2D band position (ω_{2D}), (e) intensity ratio of Co to G band (I_{Co}/I_G), (f) intensity ratio of 2D to G band (I_{2D}/I_G), and (g) ω_{2D} versus ω_G band determining the defect types [i.e. residual or neutral versus charged (*p*- or *n*-type)].

at lower wavenumber correspond to the deformation modes of the metal–oxygen chain of Co–O–Co in the CoO cubic lattice. As the cobalt atom is about five times heavier than the oxygen atoms, the vibrations of the Co–O groups are supposed to involve mainly the oxygen atoms. The peak at 482.4 cm^{-1} is broad due to smaller crystallite size, whereas the peak at 690 cm^{-1} is slightly asymmetric. The asymmetry may be attributed to possible secondary crystalline phase CoO and/or Co_2O_3 apparent in Fig. 8c. The vibration band located at 482 cm^{-1} is attributed to the vibration of cobalt species (Co^{3+}-O^{2-}) in the octahedral site of Co_3O_4. The lower relative intensity for each vibrational mode may also be due to the confinement of phonons by some crystal defects caused by Co^{4+} vacancies and oxygen-related defect sites, resulting in the decay of phonons and destruction of conservation of phonon momentum. The Raman peak intensity at 620 cm^{-1} tends to disappear with smaller diameters, because, when the nanoparticle size decreases, the number of surface atoms increases rapidly, having a large number of dangling bonds, and the coordination is incomplete, which can lead to crystal defects and the partial breakdown of the Raman selection rules.

Raman spectra of graphene-supported CoO and Co_3O_4: The optical appearance of the hybrids is highly homogeneous especially with a rough amberish dust or blackish surface spotted with dark green islands. The Raman spectra are taken on different points of the surface for the relatively low loaded cobalt oxides presented in Fig. 8e. The difference in surface composition going from one point to another is apparent, albeit marginal. The CoO_x layer was thin enough for GO and rGO supports to be recognized and measured suitably. The first- and second-order Raman spectra of rGO and GO films show two characteristic intense peaks, a G band at ~1580 cm^{-1} and a 2D band at ~2670 cm^{-1}, which are assigned to the in-plane vibrational mode (E_{2g} phonon of the C_{sp2} atoms at the Brillouin zone center, $k \sim 0$) and the intervalley double resonance scattering of two TO phonons around the K-point of the Brillouin zone, respectively.[69] Here, we refer to the 2D band to signify that it is the second-order or first overtone of the D band. Other important features at ~1340 cm^{-1} are a defect-induced peak assigned to the D band activated by the intervalley double-resonance Raman process and the combination mode of D and G modes (D + G band) at 2920 cm^{-1}.[69,76] Commonly, the frequency-integrated intensity ratio of D to G band (I_D/I_G) can serve as a convenient semi-quantitative measure of

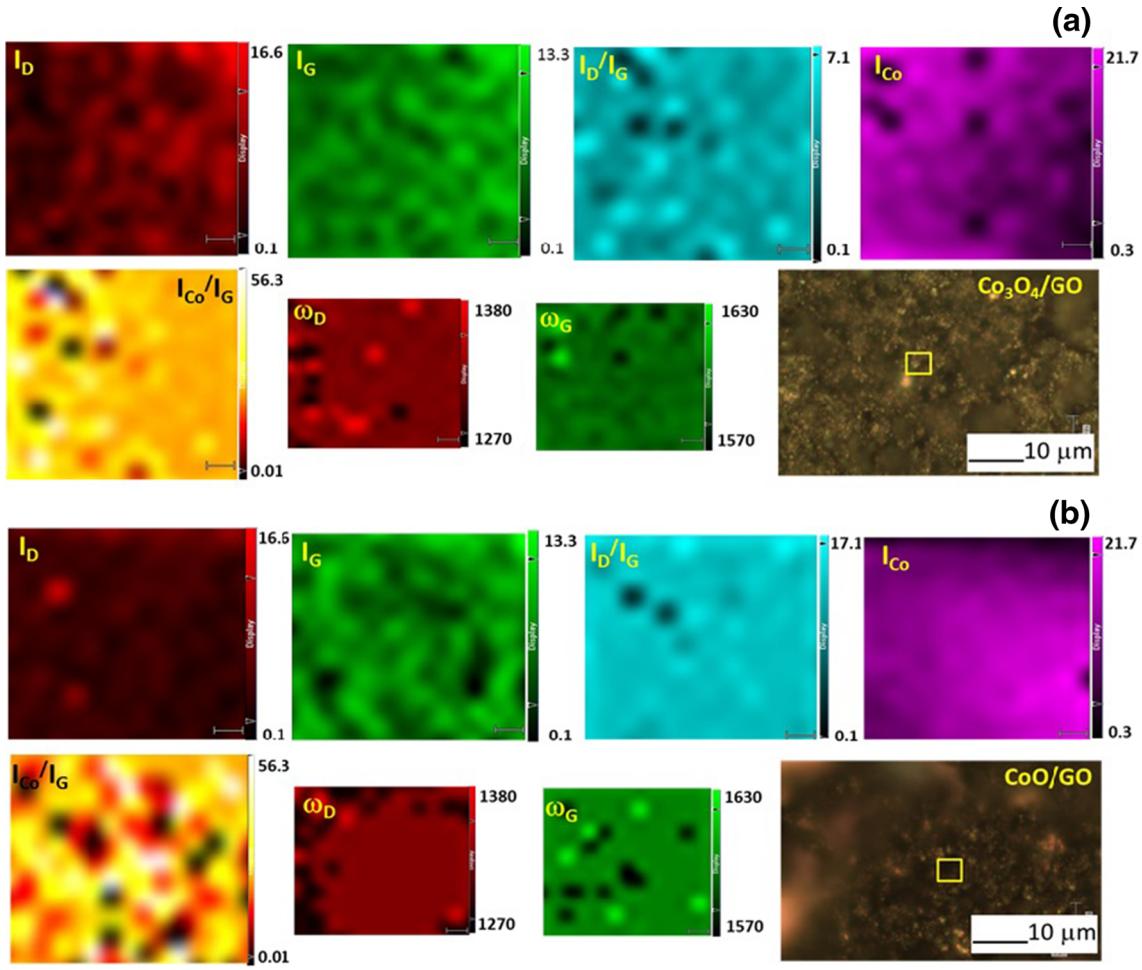

Fig. 10. (Color online). Raman mapping of representative hybrid samples of (a) CoO/GO, (b) Co_3O_4/GO, (c) CoO/rGO, and (d) Co_3O_4/rGO in terms of intensity distribution of the D, G, 2D and Co bands and their ratio with the G band. Corresponding optical micrographs taken with white-light or broadband light are also shown. The elemental distribution of cobalt-rich and carbon-rich regions are apparent and possible surface charge transfer via plot of the 2D band to the G band position for (c) the CoO/rGO hybrid. The black regions represent either the substrate (SiO_2) or lower bound as shown by the scale bars adjacent to every Raman spectra-generated map.

defects concentration in graphitic materials and the size of the sp^2 C domains which is found to increase on the reduction of GO.[69] All the Raman spectra are normalized with respect to the G band intensity for comparative analysis. The Raman spectra are analyzed in terms of D, G and 2D band positions (ω_D, ω_G and ω_{2D}), the ratio of D to G (I_D/I_G), G to 2D (I_G/I_{2D}), Co to G (I_{Co}/I_G), as well as 2D versus G band position (ω_{2D} versus ω_G), where the latter is used to determine the nature or type of defects (the results are summarized in Fig. 9). For GO-based hybrids, the D band varies between 1345 cm^{-1} and 1325 cm^{-1} and the G band is between 1593 cm^{-1} and 1581 cm^{-1}, the D band for rGO-based systems is between 1330 cm^{-1} and 1332 cm^{-1}, and the G band varies between approximately 1605 cm^{-1} and 1592 cm^{-1} which is within the spectral resolution. On the other hand, the 2D band changes rather strongly with cobalt oxides on GO (2630–2617 cm^{-1}) and rGO (2650–2625 cm^{-1}) supports. The frequency-integrated intensity ratios (I_D/I_G and I_{2D}/I_G) of the D and 2D bands with respect to the G band show strong dependence with cobalt oxides on GO (0.5–1.5 and 0.1–0.4) and rGO (1.1–1.4 and 0.1–0.3) supports. The I_D/I_G follows an inverse proportion relationship to the fourth power of the laser energy, i.e. E_L^{-4} (or, λ_L^4) relationship. This relationship was previously reported in a Raman study of nanographite.[76,77] Alternatively, on the basis of the calculation of Raman scattering theory, matrix elements associated with the double resonance processes of the D band show a dependence of E_L^{-4} for nanographite.[76] For the 2D band, it is predicted to have an excitation energy dependence of E_L^{-3}.[78]

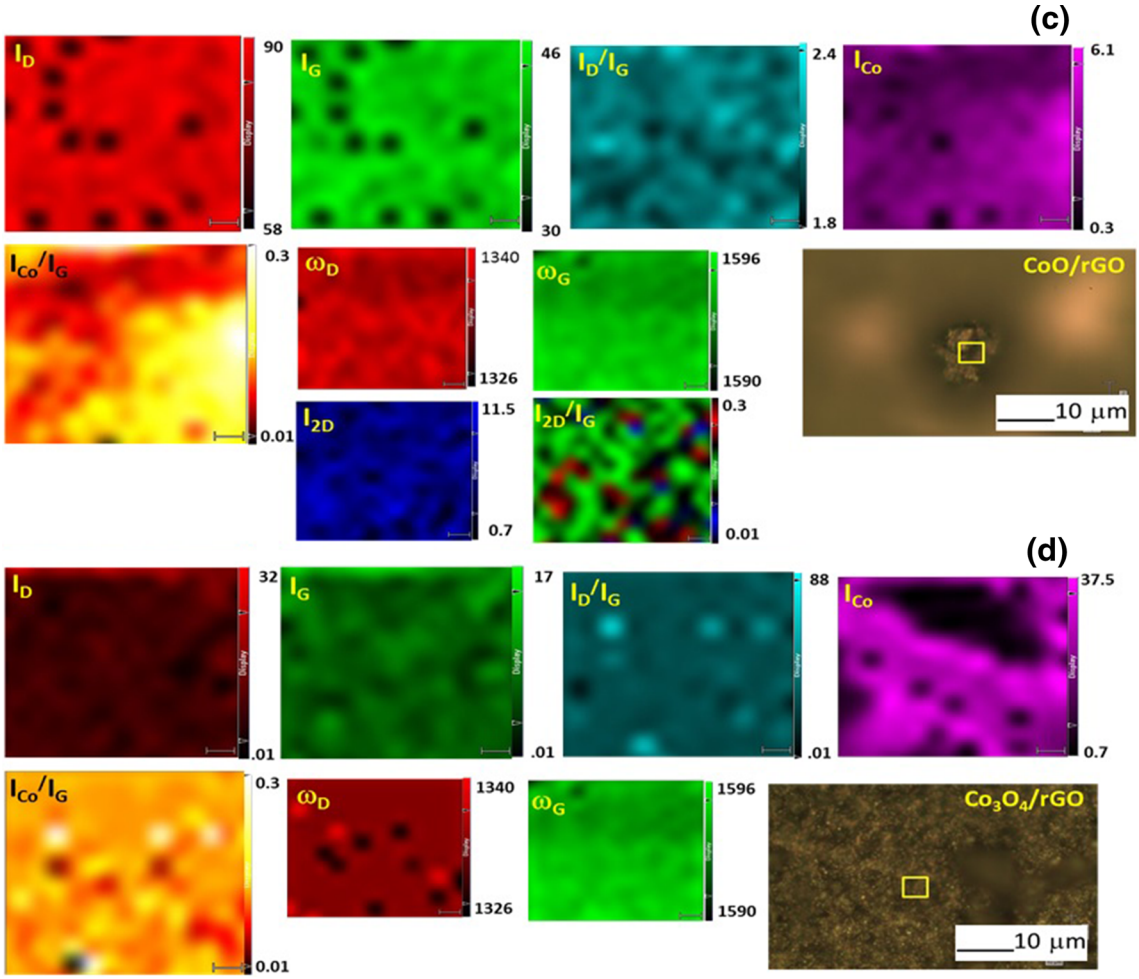

Fig. 10. continued.

For the I_{Co}/I_G ratio, while it is 10–15 for most of the GO-based samples, possibly this large value is due to a thicker Co area, the rGO-based samples have lower values of 0.5–3. We also made an attempt to determine the nature of the defects by plotting the 2D band position with the G band position (see Fig. 9g). It is safer to say that the defects are of residual- or *p*-type for GO-based hybrids, while rGO-based hybrids exhibited *n*-type defects (i.e. the G band increases and the 2D band decreases).[79] The sensitivity of Raman analysis of these samples is one of the reasons for the difference between the Raman and XRD phase identifications. The XRD diffractograms revealed the presence of only bulk phases, whereas the Raman spectra allowed the identification of local surface cobalt oxides species.

The Raman mapping of the hybrid samples is shown as representative examples indicative of the surface or spatial uniformity/inhomogeneity, thus an indirect measure of elemental composition (sp^2 C or C rich versus Co-rich) similar to EDS (see Fig. 10). The sharpness and *almost* uniform intensity maps of D-, G- and Co-related bands (corrected for baseline while generating the maps) contoured at the boundary of graphene sheet nanodomains, nanowalls and layers are reflective of a higher degree of crystalline order and thus the intrinsic nature of the graphene oxide, reduced graphene oxide and cobalt oxide nanoparticulates supported upon them. It is noteworthy that the ratio of intensity maps of the Co peak to the G peak (referred to as sp^2 C) provides some avenue to local charge transfer features that are primarily a consequence of strong electronic/structural coupling of CoO and Co_3O_4 with functional groups associated with graphene derivatives. This has a strong influence on the electrochemical reactivity discussed below in terms of electrocatalytic activity relevant to Co_3O_4.[80,81] While cobalt oxides by themselves are limited (or even inactive electrocatalytically), their loading on conductive nanocarbon supports facilitate electrocatalysis. However, upon their loading on graphene supports, this enables surface hybridization thus activating chemical bonds and enhancing acitivity/

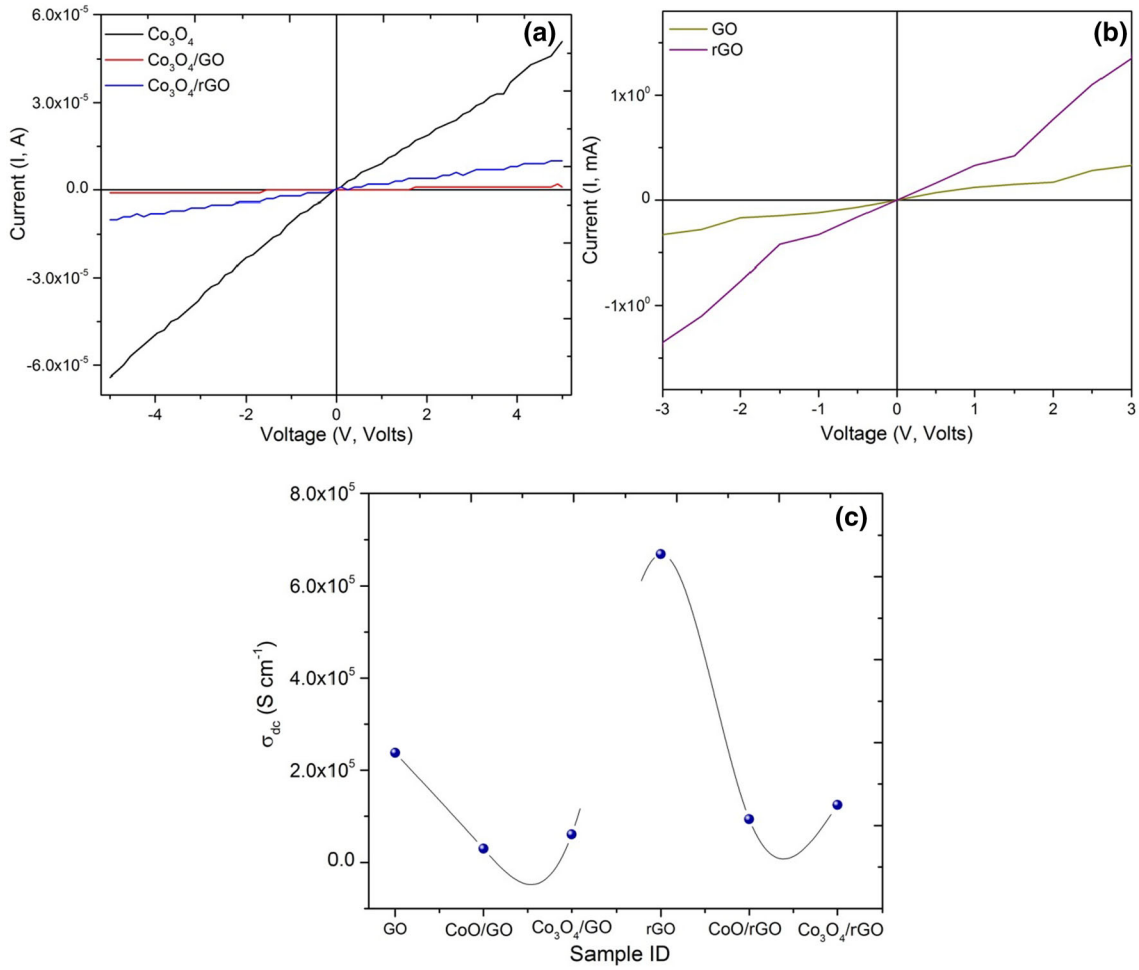

Fig. 11. (Color online). The room temperature electrical property (a, b) *I–V* (current–voltage) curves and (c) electrical conductivity (σ_{dc}) for all the samples.

reactivity compared with those of pure components or primitive traditional composites. Furthermore, the activity depends upon the C versus Co_xO_y loading concentrations, and the graphene–cobalt oxide hybrids can lead to a good bifunctional catalytic activity in alkaline solution namely, oxygen reduction (ORR) and oxygen evolution (OER) reactions.[82] These are the key points for various renewable energy technologies, including fuel cells, metal–air (O_2) batteries, and water splitting. As it is known that Co_3O_4 has the normal spinel structure $Co^{2+}(Co^{3+})_2O_4$, experimental and theoretical measurements have demonstrated that the three low Miller index planes ({100}, {110} and {111}) of such metallic oxide particles with fcc structure differ not only in the surface atomic density but also in the electronic structure, geometric bonding and chemical and electrochemical reactivity. As a result, those planes have different surface energies, following the order $\gamma\{111\} < \gamma\{100\} < \gamma\{110\}$, which is closely parallel to the catalytic activities for CO and CH_4 oxidation.[83–86] For catalyzing CO oxidation, the CO molecule interacts preferably with the surface Co^{3+} cations, which is the only favorable site for CO adsorption, as confirmed theoretically[87,88] and shown experimentally for Co_3O_4.[89] The oxidation of the adsorbed CO then occurs by abstracting the surface oxygen that had been coordinated with the Co^{3+} cations. The partially reduced cobalt site, i.e. Co^{2+} cation with a neighboring oxygen vacancy, is re-oxidized by a gas-phase oxygen molecule or the oxygen from the water molecules in aqueous electrolyte back to the active Co^{3+} form. Consequently, the surface Co^{3+} cations are regarded as the active sites for CO oxidation, whereas the surface Co^{2+} cations are almost inactive. It is known that, in the Co_3O_4 crystal structure, the {001} and {111} planes contain only Co^{2+} cations, while the {110} plane is composed mainly of Co^{3+} cations. This scenario has been proved by surface differential diffraction studies concluding that the Co^{3+} cations are present solely on the {110} plane. Similarly, in our own experiment with the Co_3O_4/rGO composite electrode, while the electrochemical activity of the

Co_3O_4/rGO (and Co_3O_4/GO) composites for CO (carbon monoxide) oxidation is by no means optimized, we are tempted to say that through our findings the Co_3O_4 with the predominantly {110} exposed surfaces may have higher electrochemical activity for CO oxidation than the sole six {100} exposed surfaces. In sharp contrast, the Co_3O_4 enclosed by the eight {111} facets on the rGO and GO sheets is expected to exhibit the highest electrochemical activity among the four Co_3O_4/graphene hybrid electrodes. Theoretically, it is predicted that the electron contribution of Co_{3d} states prevail, while the other are the contributions of O_{2p} oxygen states. The contributions of occupied C_{2p} states at the Fermi level turn out to be smaller by 2 orders of magnitude than the oxygen contributions, having the smaller value of 0.008, albeit nonzero. The latter is consistent with the graphene conductivity never being smaller than the minimum value of the quantum conductivity unit. Thus, it is conceivable to presuppose that graphene islands can retain their unique properties in the CoO_x (001)/graphene system, which makes the basis for carbon-containing electronic and magnetic electronic devices.[90,91] The other implications of this study stem from the direction of the nano-electronic and spintronic devices, i.e. hetero-interfaces of the graphene/(ferromagnetic metal or oxide) instead of nanomagnetic *p*-type semiconductors or traditional metal. It is ideal for spintronics due to a small spin–orbital interaction as well as a vanishing nuclear magnetic moment of the carbon atom.

Analogous to spectroscopic studies, electrical property measurements could also provide complementary facile information on metal oxide–graphitic interfaces including dc electrical conductivity (σ_{dc}) of hybrids. Figure 11 provides room temperature I–V measurements determining two-terminal device resistance R_{2t} and the corresponding σ_{dc}. A few noteworthy interesting features from Fig. 11 are (1) qualitatively, the I–V curves show quasi-semiconducting behavior for graphene derivatives and almost ohmic or linear behavior for all of the hybrid films showing the higher resistance for Co_3O_4/GO and the lower for Co_3O_4/rGO as expected, (2) σ_{dc} of rGO was higher by almost one order of magnitude (7×10^5 S-cm^{-1}) as compared with GO (0.1×10^5 S cm^{-1}), and, finally, (3) σ_{dc} of both rGO- and GO-supported hybrids decrease by a similar magnitude with their presence as anticipated. All these results confirm the successful synthesis of relatively optimized loaded cobalt oxide polymorphs on graphene derivatives as supports, forming nanoscale hybrids. Moreover, while the materials studied here are promising for applications in electrochemical energy storage and conversion systems and electrocatalysis, systematic electrochemical measurements are being performed to confirm this and will be published in the near future.

CONCLUSIONS

In summary, we report the development of inorganic hybrids prepared by coating the surface of nanosheets of graphene derivatives with a thin layer of nano-/micro-cobalt oxide polymorphs, i.e. CoO [Co(II)] and Co_3O_4 [Co(II, III)]) which laid the groundwork for a broad range of environmental and energy applications as high-performance advanced electroanalytical platforms. It was found that this facile approach afforded strong chemical/physical attachment and is expected to have coupling between the pseudocapacitive transition metal oxides and supercapacitive graphene with reasonable areal density of tailored interfaces. The much anticipated resulting in large interfacial areas enhances energy and charge transfer processes, improving the electrochemical and electrocatalytic activity/reactivity. The superior characteristics of these materials are generated by synergistic charge transfer processes at the interface of the two components. By employing a range of complementary structural and physical property characterization techniques, we gained insights into the nature of carbon and cobalt and/or oxide elemental interfaces. The following are the key results summarized asfollows. (1) SEM allowed to observe surface morphology of GO and rGO that appeared to be 'cringed' paper or nanosheets and the nano-/micro-particles of CoO (and Co_3O_4) are physically adsorbed and well dispersed within the sheets/vertical walls of GO and rGO (2) TEM also allowed us to observe the surface morphology at nanoscale and helped to determine GO sheet thickness and particle size distribution along with SAED patterns depicting GO (rGO) rings and diffraction spots of polycrystalline CoO (and Co_3O_4). (3) XRD displayed characteristic cobalt oxide polymorphs peaks along with GO (and rGO) peaks in hybrids, thus providing an average structure. (4) RS showed characteristic GO (and rGO) and CoO (and Co_3O_4) Raman bands in hybrids showing the successful formation of tailored interfaces crucial for applied electrochemistry. It also provided local charge transfer owing to physically (or chemically) adsorbed cobalt oxide on graphene supports, highlighting the surface structure, local charge transfer and attribution of the interfaces. Raman maps allowed the determining of the distribution of C and Co corroborating the formation of hybrid systems. (5) Lastly, room temperature electrical property exhibited the semiconducting nature of the materials studied.

ACKNOWLEDGEMENTS

The author (S.G.) gratefully acknowledges financial support in parts from WKU Research Foundation for start-up funds and NSF KY EPSCoR RSP Grant (#3048111713-15-240). The authors (S.G and S.B.C) also thank P. Norris (Advanced Materials Institute, WKU), B. McDonald for AFM and XRD training and Dr. J. Andersland for some of the SEM/EDS and TEM

measurements and Dr. J. Jasinski (Conn Center for Renewable Energy, University of Louisville, KY) for electron diffraction data processing.

REFERENCES

1. A.K. Geim and K.S. Novoselov, *Nat. Mater.* 6, 183 (2007).
2. S. Gupta, E. Heintzman, and J. Jasinski, *J. Electron. Mater.* 43, 3458 (2014).
3. Y. Zhang, Y.-W. Tan, H.L. Stormer, and P. Kim, *Nature* 438, 201 (2005).
4. M.D. Stoller, S. Park, Y. Zhu, J. An, and R.S. Ruoff, *Nano Lett.* 8, 3498 (2008).
5. C. Lee, X.D. Wei, J.W. Kysar, and J. Hone, *Science* 321, 385 (2008).
6. F. Liu, C.W. Lee, and J.S. Im, *J. Nanomaterials* 642915, 1 (2013).
7. J. Hou, Y. Shao, M.W. Ellis, R.B. Moore, and B. Yi, *PCCP* 13, 15384 (2011).
8. B. Seger and P.V. Kamat, *J. Phys. Chem. C* 113, 7990 (2009).
9. S. Gupta and A. Irihamye, *AIP Advances* 5, 037106 (2015).
10. K.P. Loh, Q.L. Bao, P.K. Ang, and J.X. Yang, *J. Mater. Chem.* 20, 2277 (2010).
11. K.P. Loh, Q. Bao, G. Eda, and M. Chowalla, *Nat. Chem.* 2, 1015 (2014).
12. G. Eda and M. Chowalla, *Adv. Mater.* 22, 2392 (2010).
13. F. Schwierz, *Nat. Nanotechnol.* 5, 487 (2010).
14. P. Blake, P.D. Brimicombe, R.R. Nair, T.J. Booth, D. Jiang, F. Schedin, L.A. Ponomarenko, S.V. Morozov, H.F. Gleeson, E.W. Hill, A.K. Geim, and K.S. Novoselov, *Nano Lett.* 8, 1704 (2008).
15. A.J. Du, Z.H. Zhu, and S.C. Smith, *J. Am. Chem. Soc.* 132, 2876 (2010).
16. S.G. Khandalkar, J.L. Gunjalkar, C.D. Lokhande, and O.-S. Joo, *J. Alloys Comp.* 478, 594 (2009).
17. I.V. Pavlidis, T. Vorhaben, D. Gournis, G.K. Papadopoulos, U.T. Bornscheuer, and H. Stamatis, *J. Nanoparticle Res.* 14, 842 (2012).
18. L. Zhang, J. Xia, Q. Zhao, L. Liu, and Z. Zhang, *Small* 6, 537 (2010).
19. J.T. Wei Wang, J.M. Ball, E.M. Barea, A. Abate, J.A.A. Webber, J. Huang, M. Saliba, I.M. Sero, J. Bisquert, H.J. Snaith, and R.J. Nicholas, *Nano Lett.* 14, 724 (2014).
20. M. Liu, R. Zhang, and W. Chen, *Chem. Rev.* 114, 5117 (2014).
21. Q. Zhang, E. Uchaker, S.L. Candelaria, and C. Guozhong, *Chem. Soc. Rev.* 42, 3127 (2013).
22. B.E. Conway, V. Bliss, and J. Wojtowicz, *J. Power Sources* 66, 1 (1997).
23. L. Nyholm, G. Nyström, A. Mihranya, and M. Strømme, *Adv. Mater.* 23, 3751 (2011).
24. A.H.C. Neto, F. Guinea, N.M.R. Peres, K.S. Novoselov, and A.K. Geim, *Rev. Mod. Phys.* 81, 109 (2009).
25. D.A. Dikin, S. Stankovich, E.J. Zimney, R.D. Piner, G.H.B. Dommett, G. Evmenenko, S.T. Nguyen, and R.S. Ruoff, *Nature* 448, 457 (2007).
26. J.T. Robinson, M. Zalalutdinov, J.W. Baldwin, F.K. Perkins, E.S. Snow, Z. Wei, P.E. Sheeshan, and B.H. Houston, *Nano Lett.* 8, 3441 (2008).
27. J.T. Robinson, F.K. Perkins, E.S. Snow, Z. Wei, and P.E. Sheeshan, *Nano Lett.* 8, 3137 (2008).
28. X. Zuo, S. He, D. Li, C. Peng, Q. Huang, S. Song, and C. Fan, *Langmuir* 26, 1936–1939 (2010).
29. C. Jafta, F. Nkosi, L. Roux, M. Mathe, M. Kebede, K. Makgopa, Y. Song, D. Tong, M. Oyama, N. Manyala, S. Chen, and K. Ozoemena, *Electrochim. Acta* 110, 228 (2013).
30. J. Xiao, Q. Kuang, S. Yang, F. Xiao, S. Wang, and L. Guo, *Scientific Reports* 3, 2300 (2013).
31. S. Gupta, M.M. van Meveren, and J. Jasinski, *J. Electron. Mater.* 44, 62 (2015).
32. J.A. Roger and Y.G. Huang, *Proc. Natl. Acad. Sci. USA* 106, 10875 (2009).
33. D.H. Kim, N. Lu, R. Ma, Y.S. Kim, R.H. Kim, S. Wang, J. Wu, S.M. Won, H. Tao, and A. Islam, et al., *Science* 333, 838 (2011).
34. N. Mahmood, C. Zhang, H. Yin, and Y. Hou, *J. Mater. Chem. A* 2, 15 (2014).
35. P. Simon and Y. Gogotsi, *Nat. Mater.* 7, 845 (2008).
36. M. Inagaki, H. Konno, and O. Tanaike, *J. Power Sources* 195, 7880 (2010).
37. V.V.N. Obreja, *Physica E* 40E, 2596 (2008).
38. E. Frackowiak and F. Béguin, *Carbon* 39, 937 (2001).
39. W. Sugimoto, K. Yokoshima, Y. Murakami, and Y. Takasu, *Electrochim. Acta* 52, 1742 (2006).
40. C. Zhu, S. Guo, Y. Fang, L. Han, E. Wang, and S. Dong, *Nano Res.* 4, 648 (2011).
41. M. Mecklenburg, A. Schuchardt, Y.K. Mishra, S. Kaps, R. Adelung, A. Lotnyk, L. Kienle, and K. Schulte, *Adv. Mater.* 24, 3486 (2012).
42. M.H. Chakrabarti, C.T.J. Low, N.P. Brandon, V. Yufit, M.A. Hashim, M.F. Irfan, J. Akhtar, E. Ruiz-Trejo, and M.A. Hussain, *Electrochim. Acta* 107, 425 (2013).
43. S. Gupta, C. Price, and E. Heintzman, *J. Nanosci. Nanotech.* 15, 1 (2015).
44. Q. Guan, J. Cheng, X. Li, B. Wang, L. Huang, F. Nie, and W. Ni, *Sci. Rep.* 5, 10017 (2015).
45. Y. Liang, Y. Li, H. Wang, and H. Dai, *J. Am. Chem. Soc.* 135, 2013 (2013).
46. J. Zhang, J. Jiang, and X.S. Zhao, *J. Phys. Chem. C* 115, 6448 (2011).
47. J. Attenburrow, A.F.B. Cameron, J.H. Chapman, R.M. Evans, B.A. Hems, A.B.A. Jansen, and T. Walker, *J. Chem. Soc.* 1094 (1952).
48. N.N. Greenwood and A. Earnshaw, *Chemistry of the Elements*, 2nd ed. (Oxford: Butterworth-Heinemann, 1997), p. 1118.
49. G. Aminoff, *Z. Kristallgr.* 64, 475 (1927).
50. J. Coraux, L. Marty, N. Bendiab, and V. Bouchiat, *Acc. Chem. Res.* 46, 2193 (2013).
51. V. Sridharm, H.-J. Kim, J.-W. Jung, C. Lee, S. Park, and I.-K. Oh, *ACS Nano* 6, 10562 (2012).
52. T. Kyotani, K. Suzuki, H. Yamashita, and A. Tomita, *Tanso* 160, 255 (1993).
53. T. Nakajima, A. Mabuchi, and R. Hagiwara, *Carbon* 26, 357 (1988).
54. W. Scholz and H.P.Z. Boehm, *Anorg. Allg. Chem.* 369, 327 (1969).
55. M. Ding, Y. Tang, and A. Star, *J. Phys. Chem. Lett.* 4, 147 (2013).
56. R. Narayanan, H. Yamada, M. Karakaya, R. Podila, A.M. Rao, and P.R. Bandaru, *Nano Lett.* (2015). doi: 10.1021/acs.nanolett.5b00055.
57. X.P. Yang, Z.G. Lin, L.Y. An, W.J. Guo, and L.X. Nian, *Acta Phys. Chim. Sin.* 28, 331 (2012).
58. Q. Zhou, Z. Fu, Y. Tang, H. Zhang, and C. Wang, *Physica E* 60, 133 (2014).
59. A.N. Rudenko, F.J. Keil, M.I. Katsnelson, and A.I. Lichtenstein, http://arxiv.org/abs/1206.1222v2.
60. W. Wei, X. Cui, W. Chen, and D.G. Ivey, *Chem. Soc. Rev.* 40, 1697 (2011).
61. W. Hummers and R.J. Offeman, *Am. Chem. Soc.* 80, 1339 (1958).
62. S. Park, J. An, R.J. Potts, A. Velamakanni, S. Murali, and R.S. Ruoff, *Carbon* 49, 3019 (2011).
63. D.C. Marcano, D.V. Kosynkin, J.M. Berlin, A. Sintskii, Z. Sun, A. Slesarev, L.B. Alemany, W. Lu, and J.M. Tour, *ACS Nano* 4, 4806 (2010).
64. M. Ding, Y. Tang, and A. Star, *J. Phys. Chem. Lett.* 4, 147 (2013).
65. S. Greenwald, *Acta Crystallogr.* 6, 396 (1953).
66. W.L. Smith and A.D. Hobson, *Acta Crystallogr. B* 29, 362 (1953).
67. H. Lipson and A.R. Stokes, *Nature* 149, 328 (1942).
68. O. Zhou, R.M. Fleming, D.W. Murphy, C.H. Chen, R.C. Haddon, and A.P. Ramirez, *Science* 263, 1744 (1994).
69. A.C. Ferrari, *Solid State Commun.* 143, 47 (2007).
70. V.G. Hadjiev, M.N. Iliev, and I.V. Vergilov, *J. Phys. C: Solid State Phys.* 21, l199 (1988).
71. W.I. Roth, *J. Phys. Chem. Solids* 25, 1 (1964).

72. H. Shirai, Y. Morioka, and I. Nakagawa, *J. Phys. Soc. Japan* 51, 592 (1982).
73. H. Poulet and J.P. Mathieu, *Spectres de Vibration et Symttrie de Cristaw* (Paris: Gordon and Breach, 1970), pp. 23–45.
74. I. Rusakova, T.O. Ely, C. Hofmann, D.P. Centurion, C.S. Levin, N.J. Halas, A. Luttge, and K.H. Whitmire, *Chem. Mater.* 19, 1369 (2007).
75. C.M. Julien and M. Massot, *J. Phys.: Condens. Matter* 15, 3151 (2003).
76. L.G. Cançado, K. Takai, T. Enoki, M. Endo, Y.A. Kim, H. Mizusaki, A. Jorio, L.N. Coelho, R. Magalhaes-Paniago, and M.A. Pimenta, *Appl. Phys. Lett.* 88, 163106 (2006).
77. K. Sato, R. Saito, Y. Oyama, J. Jiang, L.G. Cancado, M.A. Pimenta, A. Jorio, G. Ge Samsonidze, G. Dresselhaus, and M.S. Dresselhaus, *Chem. Phys. Lett.* 427, 117 (2006).
78. J.S. Park, A. Reina, R. Saito, J. Kong, G. Dresselhaus, and M.S. Dresselhaus, *Carbon* 47, 1303 (2009).
79. M.W. Iqbal, A.K. Singh, M.Z. Iqbal, and J. Eom, *J. Phys.: Condens. Matter* 24, 335301 (2012).
80. X.F. Tang, J.H. Li, and J.M. Hao, *Mater. Res. Bull.* 43, 2912 (2008).
81. Y. Sun, P. Lv, J.-Y. Yang, L. He, J.-C. Nie, X. Liu, and Y. Li, *Chem. Commun.* 47, 11279 (2011).
82. W. Chaikittisilp, N.L. Torad, C. Li, M. Imura, N. Suzuki, S. Ishihara, K. Ariga, and Y. Yamaguchi, *Chem. Eur. J.* 20, 4217 (2014).
83. X.W. Xie, Y. Li, and Z.Q. Liu, *Nature* 458, 746 (2009).
84. L.H. Hu, Q. Peng, and Y.D. Li, *J. Am. Chem. Soc.* 130, 16136 (2008).
85. L. Hu, K. Sun, Q. Peng, B. Xu, and Y. Li, *Nano Res.* 3, 363 (2010).
86. J. Jansson, *J. Catal.* 194, 55 (2000).
87. P. Broqvist, I. Panas, and H. Persson, *J. Catal.* 210, 198 (2002).
88. M.C. Toroker, D.A. Kanan, N. Alidoust, L.Y. Isseroff, P. Liao, and E.A. Carter, *Phys. Chem. Chem. Phys.* 13, 16644 (2011).
89. F. Grillo, M.M. Natile, and B. Glisenti, *Appl. Catal. B-Environ.* 48, 267 (2004).
90. V.V. Ilyasov, D.A. Velikokhatskii, I.V. Ershov, I.Y. Nikiforov, and T.P. Zhdanova, *J. Struct. Chem.* 52, 849 (2011).
91. V.V. Ilyasov, D.A. Velikokhatskii, I.V. Ershov, I.Y. Nikiforov, and T.P. Zhdanova, *J. Mod. Phys.* 2, 1120 (2011).